JGR Solid Earth

RESEARCH ARTICLE
10.1029/2019JB017372

Modulation of Seismic Attenuation at Parkfield, Before and After the 2004 *M*6 Earthquake

L. Malagnini[1], D.S. Dreger[2], R. Bürgmann[2], I. Munafò[1], and G. Sebastiani[3,4,1]

[1]Istituto Nazionale di Geofisica e Vulcanologia, Rome, Italy, [2]Berkeley Seismological Laboratory, University of California, Berkeley, CA, USA, [3]Istituto per le Applicazioni del Calcolo "Mauro Picone," Consiglio Nazionale delle Ricerche, Rome, Italy, [4]Istituto "Guido Castelnuovo," Dipartimento di Matematica, Università di Roma 'La Sapienza, Rome, Italy

Abstract The crack density within a fault's damage zone is thought to vary as seismic rupture is approached, as well as in the postseismic period. Moreover, external stress loads, seasonal or tidal, may also change the crack density in rocks, and all such processes can leave detectable signatures on seismic attenuation. Here we show that attenuation time histories from the San Andreas Fault at Parkfield are affected by seasonal loading cycles, as well as by 1.5–3-year periodic variations of creep rates, consistent with Turner et al. (2015, https://doi.org/10.1002/2015JB011998), who documented a broad spectral peak, between 1.5 and 4 years, of the spectra calculated over the activity of repeating earthquakes, and over InSAR time series. After the Parkfield main shock, we see a clear modulation between seismic attenuation correlated to tidal forces. Opposite attenuation trends are seen on the two sides of the fault up to the *M*6.5 2003 San Simeon earthquake, when attenuation changed discontinuously, in the same directions of the relative trends. Attenuation increased steadily of over one year on the SW side of the San Andreas Fault, until the San Simeon earthquake, whereas it decreased steadily on the NE side of the San Andreas Fault, roughly for the six months prior to the event. Random fluctuations are observed up to the 2004 *M*6 Parkfield main shock, when rebounds in opposite directions are observed, in which attenuation decreased on the SW side, and increased on the NE side.

Key Points:
- Seismic attenuation fluctuates with periods related to solid tides and seasonal loading, indicating strong sensitivity to stress changes
- Attenuation on the opposite sides of the San Andreas Fault shows mirror-like anomalies before and after the 2004 Parkfield main shock
- Earthquake-induced damage increases the sensitivity of seismic attenuation to periodic stress fluctuations

Supporting Information:
- Supporting Information S1

Correspondence to:
L. Malagnini,
luca.malagnini@ingv.it

Citation:
Malagnini, L., Dreger, D. S., Bürgmann, R., Munafò, I., & Sebastiani, G. (2019). Modulation of seismic attenuation at Parkfield, before and after the 2004 *M*6 earthquake. *Journal of Geophysical Research: Solid Earth*, *124*, 5836–5853. https://doi.org/10.1029/2019JB017372

Received 18 JAN 2019
Accepted 25 MAY 2019
Accepted article online 4 JUN 2019
Published online 26 JUN 2019

1. Introduction

The physical mechanisms of seismic attenuation have been thoroughly investigated (O'Connell & Budiansky, 1977; Winkler et al., 1979; Winkler & Nur, 1972), demonstrating that important parameters are related to the presence of cracks (i.e., their density, connectivity, orientation, and saturation), with a strong role played by interstitial fluids. Prior to an earthquake, the development of dilatancy predicts fluctuations in crack density of crustal rocks (Gupta, 1973; Kaproth & Marone, 2013; Nur, 1972; Scholz, 2019), which can leave a signature in seismic velocities (Scholz, 2019) and consequently also in seismic attenuation.

Recent studies showed that seismic velocity (and thus attenuation) is modulated by Earth tides at multiple frequencies (12 and 24 hr; e.g., Takano et al., 2014), whereas short-period tides have been documented to modulate tremor and slow slip events in subduction zones and also at Parkfield (Hawthorne & Rubin, 2010; Nakata et al., 2008; Thomas et al., 2009, 2012; Van der Elst et al., 2016). Finally, annual stress variations from hydrological loads appear to modulate Cascadia tremor (Pollitz et al., 2013), as well as California microearthquakes (Johnson, Fu & Burgmann, 2017).

Because we are interested in precursory phenomena, and we are trying to recognize patterns on a path leading to catastrophic failure, it is very important to understand the variations of rock crack density throughout the seismic cycle (Gupta, 1973; Kaproth & Marone, 2013; Nur, 1972; Vasseur et al., 2017). Increases in crustal crack density may be induced by raising the shear stress, and/or by relaxing the normal stress, and the exact opposite is true for decreases in crustal crack density. Studies on this topic have been performed by monitoring acoustic emissions of a rock sample under stress, and Vasseur et al. (2017) showed that heterogeneous samples are characterized by a power law increase of acoustic emissions under an increasing stress, and predictable times of failure. However, in studying crustal rocks we need to take into consideration seasonal and tidal stress variations, pore fluid pressure, and thermal stress changes (Johnson et al., 2017; Wang et al., 2017). Variations of a rock's crack density are also related to other phenomena: for example, periodic 1.5–4-year fluctuations of creep rates occur along the San Andreas Fault (SAF) at Parkfield (Khoshmanesh & Shirzaei, 2018; Nadeau & McEvilly, 2004; Turner et al., 2015).

Shaking-induced damage also results in increased crack density; in contrast, fault healing reduce crack density, and each change in crack density will lead to a change in effective bulk and shear moduli, pore fluid saturation, and anelastic attenuation (O'Connell & Budiansky, 1977; Winkler & Nur, 1972). Substantial variations of crack density and pore fluid saturation are thus expected to occur in crustal rocks during the seismic cycle, and in response to other sources of time-dependent stress and deformation, including tides and seasonal hydrological loads. All the mentioned sources of variations of crack density, pore fluid saturation, and pressure should leave a signature on the seismic attenuation.

The goal of this study is to measure seismic attenuation as a function of time with high resolution (i.e., with as many time domain measurements as possible), and we do so by analyzing seismograms from SAF repeating earthquakes (Nadeau & Johnson, 1998). Repeating earthquakes rupture exactly the same set of strong patches (asperities) embedded in a creeping, weak matrix, and the use of families of co-located events minimizes the effect of random event mislocations on measurements of seismic velocity (Uchida & Bürgmann, 2019), or attenuation. Moreover, our data set contains a number of individual repeating earthquake families that are in sufficient numbers to provide a dense temporal sampling of the seismic attenuation (1,005 repeating earthquakes between 1987 and 1998, and 774 repeating earthquakes between 2001 and 2012).

Our repeating earthquakes have waveforms with correlation coefficients >0.98, which guarantees that all events in a specific family are effectively co-located and have highly similar focal mechanisms. Co-location helps reduce the error bars on attenuation measurements because seismic waves repeatedly travel along the same paths, allowing smaller uncertainties in the results of our regressions. However, no assumptions are made about the special characteristics of the seismic sources used for this study. The only simplifying assumption we implicitly make is that the two sides of the SAF are laterally homogeneous. We believe this is justifiable, since we sample a relatively narrow zone along the SAF, and consider effects relative to a virtual path length of only 8 km, generally very close to (i.e., at a very shallow angle with) the fault surface (see later).

We calculate seismic attenuation by means of a spectral ratio technique, which automatically eliminates the instrument responses, as well as everything that affects the sites and sources in our regressions, including the long-term aging process that inevitably affects the geophones. Because we compute spectral ratios within moving time windows, in the hypothesis that the aging of the geophones is the same for all instrument, aging has no effects on our measurements.

2. Description of Data

Our data set comprises a total of 38,124 selected waveforms recorded at 12 borehole stations of the High Resolution Seismic Network (HRSN; see Figure 1; HRSN, 2014). The HRSN is actually composed of 13 borehole sensors, buried at depths between 73 and 572 m (e.g., Malagnini & Dreger, 2016), and is operated by the Berkeley Seismological Laboratory. One of the available recording sites (station GHIB) was excluded from the present study because it is too far from the center of the HRSN.

Our seismograms are from 1779 repeating earthquakes, divided in 165 clusters (Figure 1); the seismic events are from a catalog maintained by Robert Nadeau that also contains data used by Nadeau and Johnson (1998). The same data set used here has already been studied with a similar technique by Malagnini and Dreger (2016), who provided the average source parameters of all events (e.g., the individual seismic moments).

Here we focus on the different characteristics of crustal wave propagation of the two sides of the SAF, so that each side of the fault is investigated separately and independently from the other. We obtain such division and independence by separating the seismograms recorded at stations located on the Pacific side from the ones recorded by stations on the North American side of the SAF, the two subsets of waveforms being generated by the same set of sources. By doing so we are able to focus on differences in wave propagation between the two sides of the SAF.

Seismograms extracted from the repository of the Northern California Earthquake Data Center belong to two different time windows: Epoch 1 runs from 1987 to mid-1998 and Epoch 2 from 2001 to 2012. Although Epoch 2 runs up to present, our catalog of repeating earthquakes is complete up to 2012.

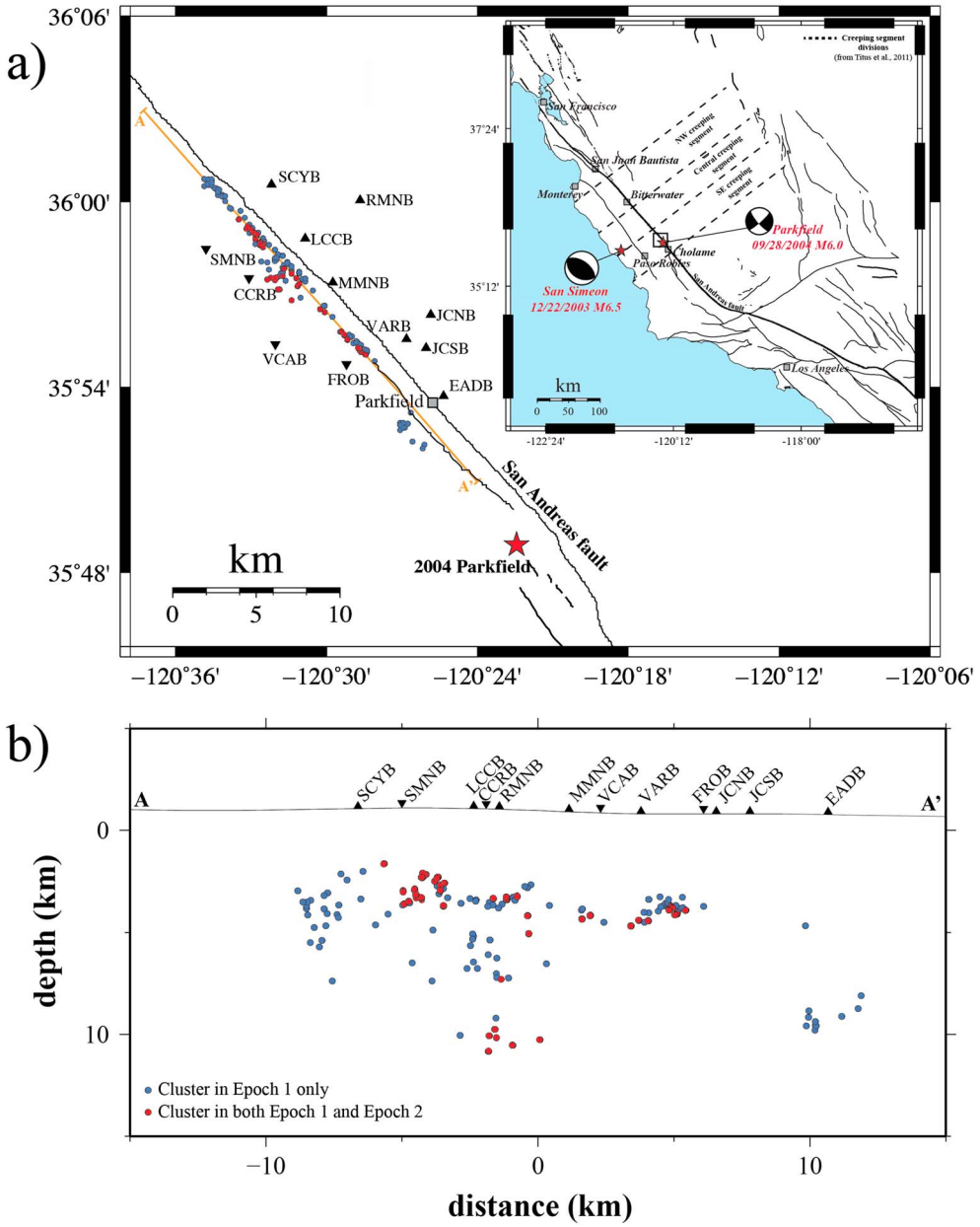

Figure 1. Map of earthquake locations and cross section. (a) Map of the investigated region showing the line of the vertical cross section A-A′, shown in (b), indicating the clusters for which we have information for both Epoch 1 and Epoch 2 (red dots) and the ones for which we only have information for Epoch 1 (blue dots). The map also shows the surface trace of the San Andreas Fault (SAF), and of the Southwestern Fracture zone (SWF; Langbein et al., 2005). For more clarity, station triangles in map and section are upside down for the four sites to the southwest of the SAF.

The 1,005 earthquakes belonging to Epoch 1 are the same ones that were used by Nadeau and Johnson (1998), and were collected in trigger mode at a sampling rate of 500 sps. In contrast, the 774 events belonging to Epoch 2 were detected using a cross-correlation procedure on waveforms recorded in continuous mode, at a sampling rate of 250 sps. Within an individual family, waveforms from different earthquakes recorded at the same seismic station are virtually identical, with a coefficient of correlation >0.98 (Nadeau & Johnson, 1998).

Repeating earthquakes are located in very tight clusters, a characteristic that reduces one source of uncertainty in our calculations (that is, errors in the propagation lengths are minimized due to co-location of earthquakes), and contributes to the minimization of the error bars of our results. Between the two

epochs, funding shortfalls prevented the HRSN from being active. We note that in the Nadeau catalog the seismicity appears to be offset from the SAF, and differs somewhat from the Northern California Seismic System and double-difference catalog locations (e.g., Waldhauser & Schaff, 2008). However, because we use amplitude ratios at two different hypocentral distances, a small systematic shift of the event locations has no detectable effects on our results. Seismic spectra are evenly sampled in the log space between 2 and 50 Hz, using a set of 20 frequencies.

As previously mentioned our technique is based on effective spectral ratios, which is appropriate when working with a set of instruments that was installed some 30 years ago and may well be subjected to aging, and thus to unknown distortion of the parameters that constitute the individual transfer functions. By using spectral ratios we can mitigate the effects due to changes in the instrument responses over time due to aging of the instruments. The latter may represent a serious problem, even for spectral ratios, if one decides to mix waveforms produced over very long periods of time. By using a relatively short moving time window, and assuming a common aging history for all instruments, our spectral ratios are effectively independent of aging. The moving time window is short throughout the entire analyzed period (it contains 40 consecutive events), and moves along calendar time.

3. Methods for Determining Attenuation Time Histories

Quantifying fluctuations in the average energy loss experienced by radiated seismic waves is a difficult task, because we need to measure very small differences in the amplitudes of seismic spectral ratios. Here we use a regression technique that has long been applied to ground motion studies (Bodin et al., 2004; Malagnini et al., 2000; Malagnini et al., 2011; Malagnini & Dreger, 2016; Malagnini & Munafò, 2017; Raoof et al., 1999), which relies on a stochastic tool called Random Vibration Theory (RVT; Cartwright & Longuet-Higgins, 1956). RVT allows us to use the peak values of narrow band-pass-filtered waveforms, instead of the Fourier amplitudes contained in the same frequency band. The considered peak value of a specific seismogram must occur after the *S* wave pick. The narrow band-pass filters are needed in order to make the seismograms relatively "stationary," as required by RVT, and the use of peak values maximizes the signal-to-noise ratios of our results (i.e., the attenuation time histories).

It must be clear at this point that, if we know the effective duration of the ground motion in a specified bandwidth around a central frequency f_c, starting at the *S* wave pick, RVT allows switching between the Fourier amplitude at that central frequency, and the peak value of a narrowband-filtered version of the same seismogram. As shown by Malagnini and Dreger (2016), the benefit from such switching is the ability to use the Convolution theorem on the peak values of narrowband-filtered seismograms.

RVT applies to relatively narrow band-pass filters around specific sampling frequencies, allowing the substitution of Fourier amplitudes with peak values at those frequencies (Malagnini & Dreger, 2016), and consequently a dramatic increase of the signal-to-noise ratio of our "spectral" measurement. In this study we use a moving-window analysis in which the path terms obtained from a window containing 40 consecutive events are associated to their median origin time. For each time window, at each sampling frequency, we invert for source, site, and propagation. Regressions on the peak values of narrowband-filtered versions of the original seismograms are performed independently at 20 central frequencies. Central frequencies are evenly spaced in log space between 2 and 50 Hz.

Given a central frequency (f_c), individual seismograms (horizontal and vertical) are band-pass-filtered using an eight-pole high-pass Butterworth filter with corner at $\frac{f_c}{\sqrt{2}}$, followed by an eight-pole low-pass Butterworth filter with corner at $\sqrt{2}f_c$. Peak values of the *S* waves from the *j*th source, recorded at the *i*th site, are measured on the filtered waveforms, $a_{ij}(t,f_c)$, cast in the matrix form (1), and inverted for source (SRC), path (D), and site (SITE) terms, one frequency at a time (Malagnini et al., 2000; Raoof et al., 1999):

$$A(r_{ij},f_c) = \log_{10}\left[peak\ \left[a_{ij}(t,f_c)\right]\right] = SRC_j(f_c) + D(r_{ij},r_0,f_c) + SITE_i(f_c). \quad (1)$$

In order to stabilize the inversions of equation (1), and to give a physical meaning to source and site terms, we apply the following constraints (Bodin et al., 2004; Malagnini et al., 2000; Malagnini et al., 2011; Malagnini & Dreger, 2016; Malagnini & Munafò, 2017; Raoof et al., 1999):

$$D(r = r_0, r_0, f_c) = 0, \tag{2}$$

and

$$\sum_{i=1}^{N} SITE_i(f_c) = 0. \tag{3}$$

It is important to clarify that the *i*th *SITE* term in equation (3) indicates the *i*th individual component of the ground motion; it follows that one specific station adds three site terms to the matrix (1). Constraint (3), applied to the horizontal component of the ground motion, gives the source terms a specific physical meaning; that is, the horizontal source "spectra" that would be observed at the reference distance r_0, by the average network site. In turn, the average site is the one relative to all the individual sites used in equation (3).

We reiterate that the implicit hypothesis is that the crustal volume under investigation is laterally homogeneous. In this specific case our hypothesis is easily justifiable, since the stations of the HRSN sample a very narrow zone along the SAF, and we choose to separately analyze the two sides of the SAF. Finally, in order to obtain relatively smooth propagation terms, a minimum roughness constraint is applied to the path terms (Malagnini et al., 2000). See Appendix A1 for more details on the technique.

Constraints (2) and (3) are simultaneously forced on each individual regression (that is, at each sampling frequency, because we invert one frequency at a time). Constraint (2) decouples the path term from the summation of source and site terms: the path term is a relatively smooth, decreasing function, which we force to assume a zero value (through constraint (2)) at an arbitrary reference distance. Because of constraint (2)), all the source terms must be referred at such arbitrary hypocentral distance. Together with constraint (3), which is applied to the horizontal components of the ground motion, they give a specific source term the following physical meaning: namely, the spectral amplitude of the horizontal components of the ground motion that would be recorded by the average network site, at the reference hypocentral distance ($r = r_0$). Here we use $r_0 = 4$ km.

The seismic sources (i.e., the repeating earthquakes) and the source terms of our regressions are two distinct items and should be regarded as such. In fact, the elements of the second set are measurements of the ground motions induced by the elements of the first set, in a specific attenuative environment. Seismic attenuation may be quantified by using the ground motions induced by many earthquakes: in case where the seismic attenuation varies with time, the source terms relative to the quantification of the same earthquake in two different time windows to which the event contributes must be different (assuming the same set of recording stations to which constraint (3) is applied).

Solving equation (1) may give rise to trade-offs that can be reduced by constraints (2) and (3), however not completely removed, assuming that: (a) every source is sampled by observations at a number of different distances along the propagation paths; (b) every site samples multiple earthquakes, at many different hypocentral distances; and (c) every distance along the propagation term is sampled by many sources and sites. However, source and site terms are not totally separable, in the sense that any effect that would simultaneously and systematically act upon all stations gets mapped, through constraint (3), onto all source terms.

Crustal propagation is spatially sampled by a fixed set of hypocentral distances between 2 and 20 km. In order to further reduce the regression uncertainties, for each time window of 40 events, we carry out 10 realizations of the regressions at all frequencies after removing 10% of the events, and the different results are averaged. The basic idea of this procedure, which allows us to reduce uncertainties, is the same as in other resampling techniques, that is, delete-m jackknife, and bootstrap (Efron, 1981), and/or importance sampling, Markov chain, and Monte Carlo (Madras, 2001).

At each frequency we take the ratio between the values of the term $D(r_{ij}, r_0, f_c)$ in equation (1) at a pair of arbitrary hypocentral distances: 12 km over 4 km (at all frequencies, at which they are the best-sampled and the first well-sampled hypocentral distances, respectively). The obtained ratios are assigned to the median time of occurrence of the 40 earthquakes in the specific time window. The window is then shifted forward in time by one event, and the procedure is repeated until we obtain $M = 20$ narrowband time histories (one for each sampling frequency, see Table S1 in the supporting information) for both Epoch 1 and Epoch 2.

Regarding the use of peak values of narrowband-filtered time histories, instead of the Fourier amplitudes of the ground motion in our regression, Malagnini and Dreger (2016) and Munafò et al. (2016) demonstrated the complete equivalence of the spectral ratios calculated with the two approaches in calculating the seismic moment of very small earthquakes. In terms of signal-to-noise ratios, the peak value-based technique is better than the one based on Fourier amplitudes, allowing more accurate and stable results.

The absence of crustal reflections in our data set, owing to the short distances, ensures that the observed attenuation trends are simple, which means that if we were to use different pairs of distances for our measurements, we would obtain time histories virtually identical to the ones shown here, in which the absolute amplitudes of the spectral ratios would change by a predictable shift, which remains quasi-constant as a function of time.

The fact that we are using spectral ratios further protects us from the possible trade-offs described above. However, if the crustal attenuation is affected by a sudden discontinuity (see later the effect of the San Simeon earthquake), an abrupt change in the path term affects only part of the earthquakes that are in a time window that contains the discontinuity. The net result is a light smear of the discontinuity over the entire moving window.

We expect no effects from the specific radiation patterns of the source terms, because our regressions average over all azimuth and takeoff angles, as well as over all the sources that enter the specific time window. However, as shown by Thurber et al. (2006), the mechanisms of microearthquakes at Parkfield show little variation, if any, from the dominant right-lateral strike-slip geometry of the San Andreas Fault, adding to the stability of our results and to the reduction of the associated uncertainties.

Within an individual family, our repeating earthquakes have waveforms with correlation coefficients >0.98; at a minimum, such a characteristic guarantees that all events in such families are virtually co-located, as well as having highly similar focal mechanisms. Co-location helps reducing error bars in our regressions, because seismic waves repeatedly travel along the same paths. In our computation, however, we make no assumptions about the seismic sources: not even about the similarity of their waveforms, probably their most important characteristic.

The amplitude ratios of Figures 2 and 3, $R[r_2, r_1, f_c]$, are calculated from the path terms obtained empirically. Although we strictly use only our empirical results, without interferences from any attenuation models, it may be interesting to describe how the amplitude ratios of Figures 2a, 2b, 3a, 3d, and 4a–4d could be modeled in terms of the two hypocentral distances, r_2 and r_1, of the sampling frequency, fc (Malagnini et al., 2000; Raoof et al., 1999), and of a frequency-dependent quality factor $Q(f) = Q_0(f_c)^{\eta}$:

$$R[r_2, r_1, f_c] = \log_{10}\left[\frac{g(r_2)}{g(r_1)}\exp\left[-\frac{\pi f_c}{\beta Q_0 (f_c)^{\eta}}(r_2 - r_1)\right]\right], \tag{4}$$

where $g(*)$ is a geometrical spreading function and β is the shear-wave velocity. The exponential function in equation (4) represents anelastic attenuation, where the exponent ($0 \le \eta \le 1$) accounts for its frequency dependence. Higher values of η are generally found in cratonic environments (Bodin et al., 2004), and lower values generally belong to more active regions (Malagnini et al., 2000; Raoof et al., 1999). At distances shorter than the depth of strong crustal discontinuities, the geometric spreading may be very simple, $g(r) \approx \frac{1}{r^{\gamma_1}}$, where $\gamma_1 \approx 1$, and

$$R[r_2, r_1, f_c] \approx \log_{10}\left[\frac{r_1}{r_2}\right] - \left[\frac{\pi f_c}{\beta Q_0 (f_c)^{\eta}}(r_2 - r_1)\right] \log_{10}[e]. \tag{5}$$

Because the two sides of the SAF have very different crustal structures and lithologies (Li et al., 2004; Thurber et al., 2006), data collected on opposite sides of the SAF are inverted separately. Given the geometry of the HRSN (within 10 km of the SAF; see Figure 1), the distribution of the hypocenters (3–9 km deep), and the short sampling distances used to define the amplitude ratios (12 and 4 km), the volume sampled by our regressions is very close to the fault, mostly just the damage zone of the SAF.

Some authors (Korneev et al., 2003) find that the damage zone of the SAF is very narrow and extends 100–200 m on either side of the SAF at seismogenic depths. Others (Langbein et al., 2005) suggest that the

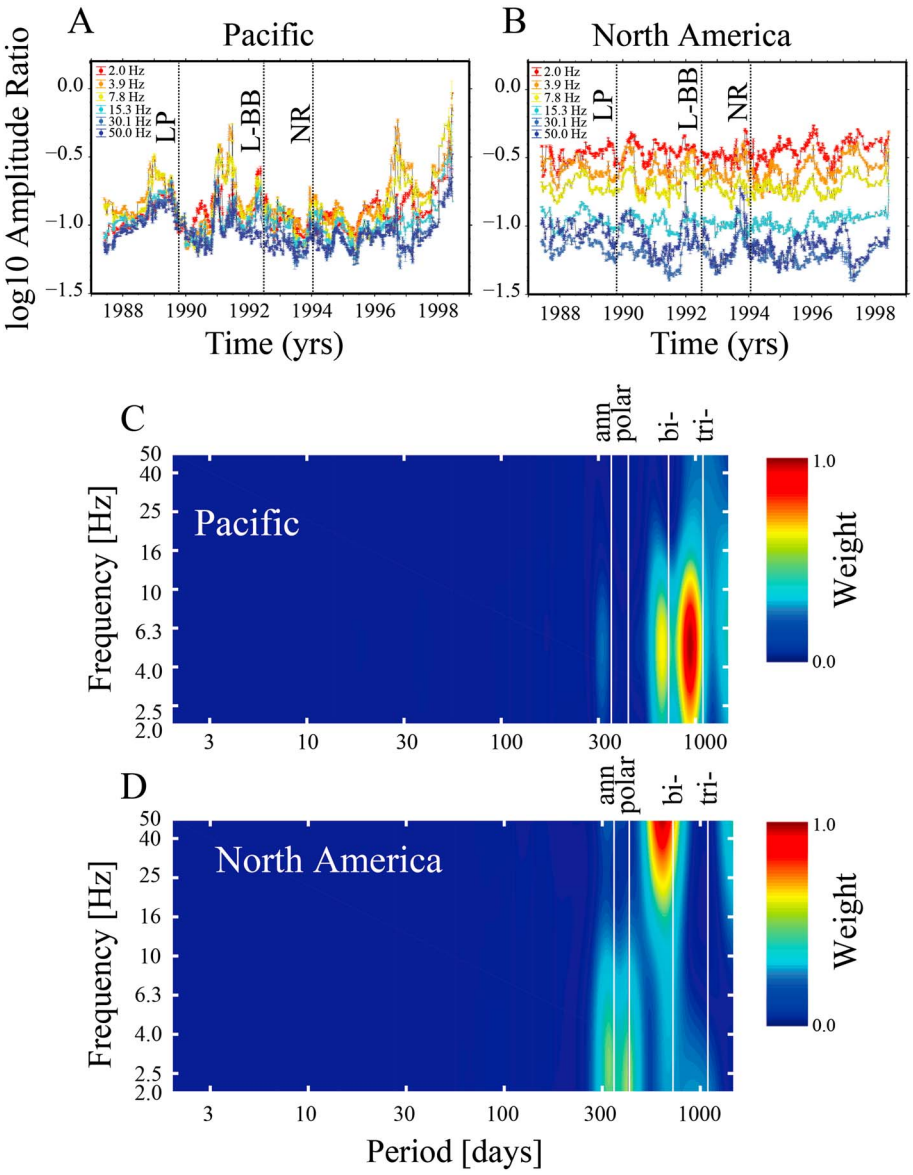

Figure 2. Epoch 1: attenuation time histories and periodograms. (a and b) Relative amplitudes as a function of time during Epoch 1, between the hypocentral distances of 12 and 4 km, for six different frequencies (out of the 20) between 2.0 and 50.0 Hz. Indicated are the times of occurrence of three major earthquakes that hit the area: Loma Prieta (LP), Landers-Big Bear (L-BB), and Northridge (NR). (a) Pacific side of the SAF. (b) North American side of the SAF. Because our technique uses the initial part of the data set to build the first data point in the attenuation time history, the derived signals in Epoch 1 begin in late 1987. There is no clear effect of the LP, L-BB, and NR events. (c and d) Periodograms calculated at all sampling frequencies: *x* axes: period (days) and *y* axes: sampling frequency (Hz). (c) Pacific side of the SAF. (d) North American side of the SAF. Indicated are the following periods: ann = annual, bi = biannual, tri = triannual, polar = 14.2-month polar tide period.

southwest fracture zone (Figure 1) may represent an upper limit for the width of the active deformation zone (1–2 km), and may indicate that on the Pacific side of the SAF the damage zone is much wider than on the North American side. Where SAFOD crosses several strands of the SAF fault zone, the damage zone is ~200 m wide at ~3-km depth (Zoback et al., 2010).

Our study aims to produce measurements with the smallest possible uncertainties. The described analysis is possible only if the signal-to-noise ratio of "spectral" amplitudes obtained of very small earthquakes (M_{max}~1.6) is well above the noise.

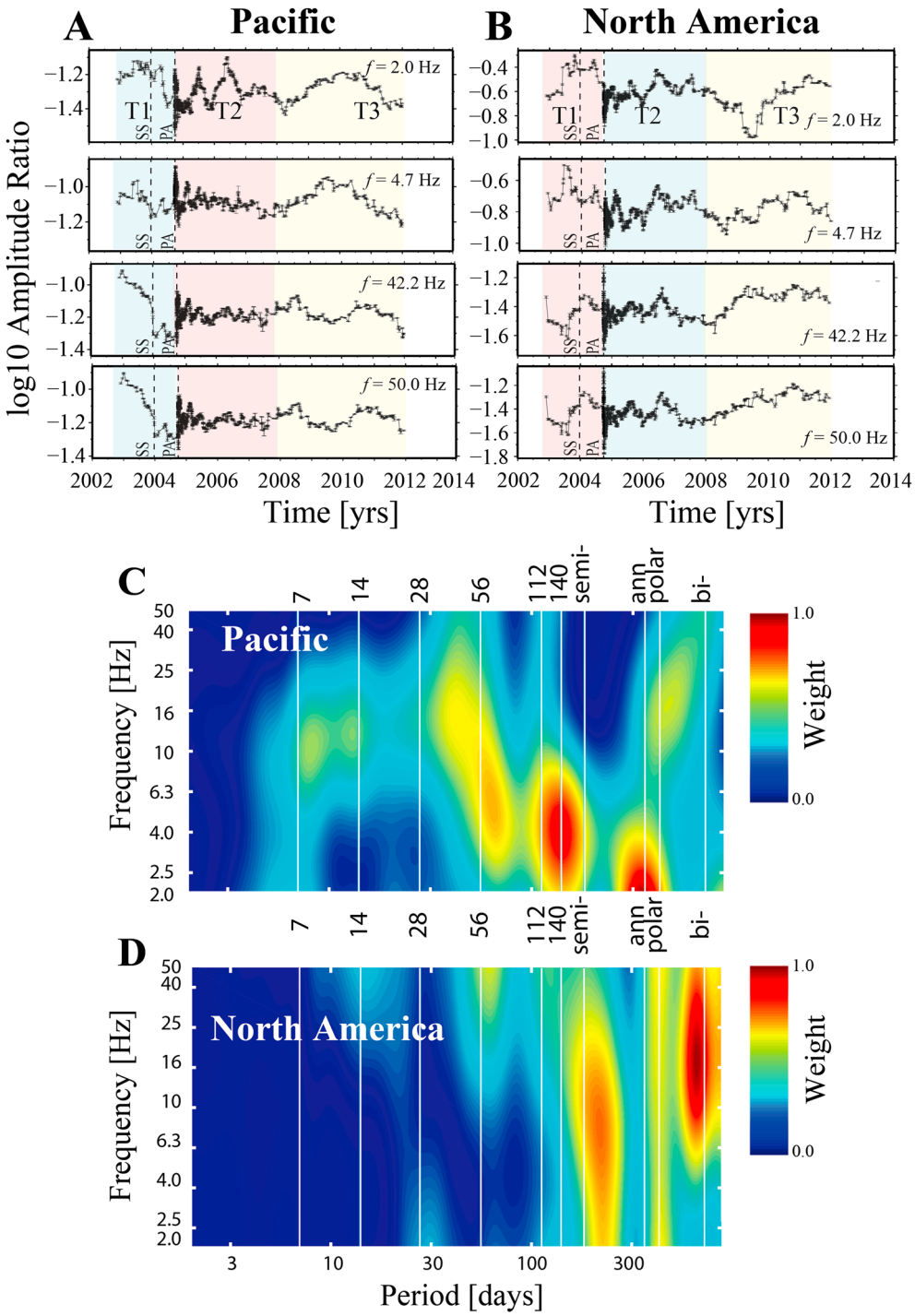

Figure 3. Epoch 2: attenuation time histories and periodograms. (a and b) Relative amplitudes as a function of time during Epoch 2, at the four frequencies indicated. Shown are the color-coded time windows called T1, T2, and T3 in the main text, as well as the times of occurrence of the San Simeon (SS) and Parkfield (PA) main shocks. (a) Pacific side of the SAF (b) North American side of the SAF. Even though the network started running in 2001, since our technique uses the initial part of the data set to build the first data point in the attenuation time history, the derived signals in Epoch 2 begin in mid-2002. (c and d) Period (*x*-axis)–frequency (*y* axis). Calculations are performed over the time window T2 + T3. (c) Pacific side of the SAF. (d) North American side of the SAF. Note the periods of the solid Earth tides (multiples and submultiples of 28 days), and the clear response to the polar tide (~14.2 months). Figures 3c and 3d contain more structure than the analogous frames in Figure 2, because of the Parkfield main shock increased the susceptibility of seismic attenuation to stress fluctuations. Indicated are the following periods: semi = semiannual, ann = annual, bi = biannual, polar = 14.2-month polar tide period.

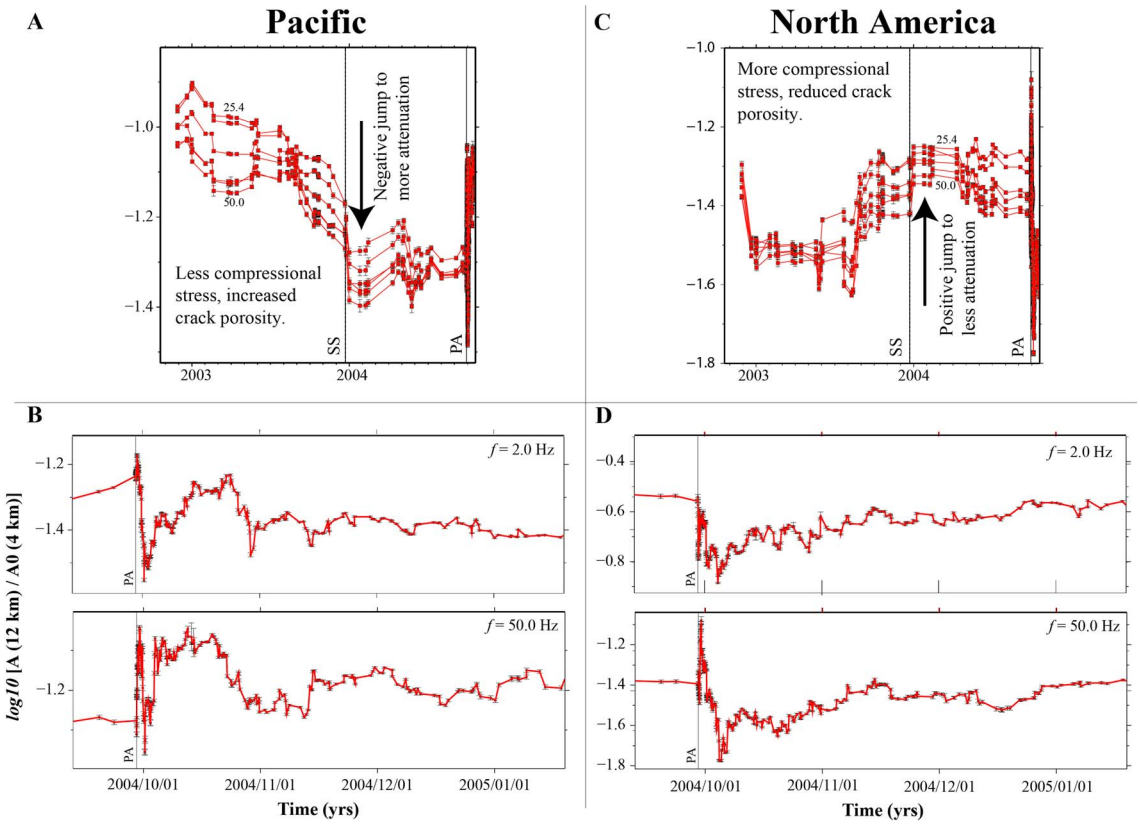

Figure 4. Zoom over attenuation time histories. (a) Zoom over time window T1, on the Pacific side of the SAF. Indicated are the occurrences of the *M*6.5 San Simeon main shock (SS) and of the Parkfield main shock (PA). (b) Early part of time window T2, Pacific side of the SAF, for two frequencies. (c) Same as (a) but for the North American side of the SAF. (d) Same as in (b) but for the North American side of the SAF.

4. Results: Attenuation Time Histories and Harmonic Analysis

We divide our attenuation-related time histories into four different segments. The first one spans the entire Epoch 1 (Figures 2a and 2b). Not only Epoch 1 lacks large local earthquakes on the small portion of the SAF at Parkfield that is directly surveyed by the HRSN, but no obvious effect from major regional earthquakes is evident; for this reason the observations made during Epoch 1 may be considered, in terms of attenuation, the "regular" behavior of the area. Three major ($M \geq 6.9$) California earthquakes during this time period (Loma Prieta, Landers, Northridge) did not produce a notable effect in the time series (see Figures 2a and 2b).

On the Pacific side of the SAF, attenuation time histories fluctuate coherently at all frequencies (Figure 2a), and they all experience very similar attenuation, consistent with $Q(f) = Q_0 f$ (i.e., the increase in Q with frequency counterbalances the fact that the energy is dissipated on a larger number of cycles; see equations (4) and (5)).

On the North American side of the SAF (Figure 2b), the time histories at high frequencies (cold colors) fluctuate in phase with their low-frequency counterparts. Moreover, the time histories are spaced apart in amplitude, consistent with a frequency-independent quality factor $Q(f) = constant$. If $Q(f) = constant$, high frequencies get attenuated more strongly than low frequencies, because the former undergo more cycles than the latter when traveling the same distance; as a result, spectral ratios at different frequencies are characterized by very different amplitudes. See equations (4) and (5). The complete set of attenuation-based time histories, at the 20 frequencies investigated in this study, between 2 and 50 Hz, are plotted in Figure S3.

For the spectral analysis of Epoch 1 we need a tool that can deal with unevenly sampled time histories, because our time samples coincide with the occurrences of individual earthquakes. Our analysis is based on Lomb-Scargle periodograms (Lomb, 1978; Scargle, 1982; Eubanks, 1999; see Figures 2c and 2d), which

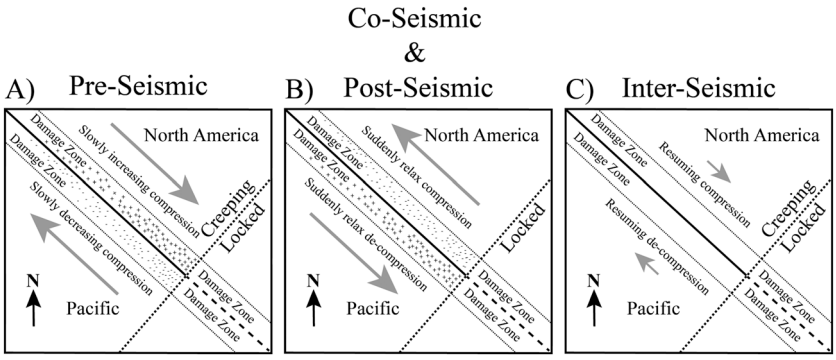

Figure 5. Simplified geometry of the fault system, schematically showing the first-order geometry envisioned that can rationalize the relation of fault slip to dilatation and attenuation on either side of the SAF. The creeping and the locked portions of the fault are indicated by adjacent continuous and dashed lines, respectively. Our data do not sample the locked portion of the SAF. (a) As the right-lateral SAF is locked SE of Parkfield (toward the SE corner of the figure), and continuously creeping NW of the locked portion (NW portion of the figure), the region close to the creeping-locked boundary increase and decrease their compression, depending on which side of the SAF they are. Relative motion is indicated by the gray arrows. It is likely that, in the preseismic period, at the end of the seismic cycle, the effects induced by increasing and decreasing compression on the crack density are more evident. (b) A stress drop is experienced due to the Parkfield earthquake: the North American side suddenly relaxes some compression, as the Pacific side suddenly relaxes some decompression. The same phenomenon continues throughout the postseismic response of the SAF. (c) In the interseismic period, the Parkfield stretch of the SAF resumes increasing compression on the North American side of the SAF, and increasing decompression on the Pacific side of the SAF.

show clear periodic variations in attenuation (annual, biannual, and triannual), especially on the North American side of the SAF. Appendices A2 A3 provide details of the different methods used in this study.

The annual periodicity of attenuation is due to seasonal stress variations caused primarily by hydrological changes of surface load. Johnson et al. (2017) studied cyclic stress changes in central and Northern California, characterized by annual periodicity; they showed that, at 8-km depth on the SAF at Parkfield, the peak-to-peak excursion of normal stress averages 1.9 kPa, and is dominated by snow and water loads in the Central Valley and in the Sierra Nevada to the NE.

Due to the presence of the *M*6 Parkfield main shock, we divide Epoch 2 into three distinct segments, hereafter defined as T1, T2, and T3, and we indicate them by different colors in Figures 3a and 3b. T1 runs from May 2002 (the beginning of Epoch 2 in our plots), when the network operations were resumed, and the occurrence of the *M*6 Parkfield earthquake on 28 September 2004. During T1, the SAF at Parkfield is locked to the SE, while it is creeping right laterally to the NW, and around the Parkfield rupture asperity (Murray & Langbein, 2006; Nadeau & Johnson, 1998). Prior to the occurrence of the 2004 main shock, the Pacific side of the SAF near Parkfield experienced decreasing compression, while the North American side of the SAF was under increasing contraction (Titus et al., 2011; see Figures 5a–5c for a simplified cartoon representation of the preseismic (Figure 5a), coseismic and postseismic (Figure 5b), and interseismic periods.

For the segment of the SAF that is responsible for the 2004 *M*6 Parkfield main shock, T1 represents the very last portion of the seismic cycle. During T1, changes in high-frequency attenuation prior to the main shock can be seen on both sides of the fault (Figures 3a, 3b, 4a, and 4b). Given the geometry of the system, and the short hypocentral distances sampled by our seismograms, fluctuations of crack density that are likely responsible for the preseismic variation in attenuation must be very close to the fault, probably within the SAF damage zone, as schematically indicated in Figure 5. Before the occurrence of the Parkfield main shock, the attenuation time histories are characterized by anomalies of opposite signs on the two sides of the SAF. Whereas an increase in attenuation clearly affects the Pacific side of the SAF, the North American side of the SAF is characterized by a moderate decrease of the seismic attenuation at high frequency.

The increasing attenuation trend experienced on the Pacific side of the SAF during T1 up to the San Simeon earthquake, together with the discontinuity corresponding to the occurrence of the earthquake, are best observed at frequencies >20 Hz, and particularly around 40 Hz (see Figures 3a, 3b, 4a, and 4b); that is, the variations in crack porosity responsible for the anomalies observed before the Parkfield main shock must have wavelengths of less than 100 m, down to approximately 10 m. In fact, Li et al. (2004) assign to the Pacific

side of the fault a shear-wave velocity of ~1.5 km/s in the first 2 km; the 20–50-Hz band (the one affected by the variations) would then be affected by structures comparable to the corresponding range of wavelength (80–30 m), or smaller.

It is intriguing that the proposed precursory anomalies seem to end with a step change due to the San Simeon earthquake, a behavior that is worthy of further investigation. Because we do not see a secular trend in Epoch 1, one possibility is that the sensitivity of seismic attenuation to small fluctuations of stress (like the one responsible for the San Simeon earthquake jump) becomes evident only in subcritical conditions (i.e., close to failure).

During T1, the SAF at Parkfield experienced a tensile normal stress change from the *M*6.5 San Simeon earthquake (Johanson & Bürgmann, 2010; Johnson et al., 2013), which leaves a clear signature in our attenuation-related measurements. Keeping in mind that more negative amplitudes mean higher attenuation, the time series plotted in Figures 3a and 3b show that at higher frequencies there is an immediate increase in attenuation on the Pacific side, and a decrease of smaller amount on the North American side (see close-up in Figures 4a and 4b). Such an opposite effect on the two sides of the SAF is not easily explained with just the static stress changes, and there are conflicting results with regards to possible accelerations in the creep rate at seismogenic depths during this time period (i.e., InSAR-derived slip transient; Khoshmanesh & Shirzaei, 2018) versus stable rates of repeater occurrence (Turner et al., 2015) and microseismicity (Aron & Hardebeck, 2009). All these findings are consistent with our idea that during T1 the Pacific side of the SAF was undergoing decreasing compression, and consequently increasing crack porosity. For an immediate effect, like the jumps of opposite signs shown in Figures 3a and 3b, it is necessary that the SAF moved, as documented by Johnson et al. (2013), who actually calculated the San Simeon earthquake-induced step-like transient creep on the SAF, in the direction of the fault motion.

Because we assume that attenuation variability is largely due to changes in crack density, we expect pressure/dilatation or normal stress changes to be most important. In fact, the decrease in normal stress from the *M*6.5 San Simeon earthquake was on the order of several tens of kilopascal on the SAF at Parkfield (Johnson et al., 2013), well above our sensitivity threshold, as inferred from the observation of the periodic modes (for example, the line at a period of 433 days, about 14.2 months (Figure 3d) most probably corresponds to the stress perturbation due to the polar tide on the SAF, which is on the order of ~100 Pa; see Johnson et al., 2017). Based on this information, the 42- and 50-Hz plots in Figure 3b tell us that, during a time period of over one year preceding the Parkfield main shock, the crust on the Pacific side for the SAF underwent a release in the compressional stress of about 20 kPa. No further decrease in compression is evident in Figures 3b and 4b between the San Simeon earthquake and the Parkfield rupture.

Time window T2 starts with the occurrence of the *M*6 Parkfield main shock, where the immediate coseismic effect was rock damage. A long postseismic effect lasted for several years after the earthquake; in terms of wave velocity changes, the postseismic period ended roughly by the beginning of 2008 (Brenguier et al., 2008), a date we assume corresponds to the end of T2 (Figures 3a and 3b). In other words, T2 represents a relatively long rebound phase (both coseismic and postseismic), in which the coseismic stress drop reverses the patterns that characterize T1, and anomalies of opposite signs are observed on the two sides of the SAF (Figures 4a and 4c).

Period T3 is a smooth anomaly, generally toward lower attenuation, characterized by the same sign on both sides of the SAF. A healing process is probably taking place during T3 within the damage zone of the SAF. In what follows, however, we treat T2 + T3 as one individual window.

The results of the Lomb-Scargle analysis on the T2 + T3 time window are shown in Figures 3c and 3d. Strong seasonal oscillations (one-year period) are evident. In addition, the perturbed system appears sensitive to Earth tides, including the 14.24-month period Chandler wobble (or polar tide; see Figures 3c, 3d and S2b but also Text S1 and Figure S1 in the supporting information on the hierarchical clustering). As we described earlier, the reason we specifically mention the Chandler wobble is because at a seismogenic depth of 8 km on the SAF at Parkfield, the related stress perturbation is very small, on the order of ~100 Pa. Because the stress sensitivity of an attenuation time history depends primarily on crack density (Niu et al., 2008), the observed change in responsiveness at these periods may be due to damage induced in the SAF damage zone by the Parkfield earthquake.

The early postseismic attenuation time histories of Figures 4a–4d show, again, opposite patterns on the two sides of the SAF: increase in attenuation in the North American side versus a decreased attenuation in the Pacific side. These opposite behaviors are consistent with a conceptual model (e.g., Figure 5) in which the elastic rebound occurring after the Parkfield *M*6 main event causes opposite effects on the crack density on the two sides of the fault.

5. Discussion

It is well established that the method used here enables the complete separation, one frequency at a time, of the first of the three terms of equation (1), representing crustal propagation ($D(r_{ij}, r_0, f_c)$), from a linear combination of the source ($SRC_j(f_c)$) and site ($SITE_i(f_c)$) terms of the same equation (Malagnini et al., 2000; Raoof et al., 1999). With a version of the same method that allows a moving time-window analysis, we determine the characteristics of wave propagation within the HRSN as a function of time.

For any practical purpose related to ground motion analyses, seismic attenuation is usually considered a time-independent characteristic of crustal rocks, or at most a quantity that weakly depends of time, so that such dependence can be neglected (Bodin et al., 2004; Malagnini et al., 2000; Malagnini et al., 2011; Malagnini & Dreger, 2016; Malagnini & Munafò, 2017; Raoof et al., 1999), favoring the use of its average properties in all situations. In general, however, seismic attenuation fluctuates due to reasons that need to be investigated in detail, such as damage, for example, as shown for the area monitored by the HRSN after the Parkfield main shock (Kelly et al., 2013).

The goal of this study is the quantification of even more subtle variations due to a number of causes, such as preseismic, coseismic, and postseismic damage; fault healing; and various periodic loads. Of special interest is the 14.2-month attenuation periodicity that characterizes the North American side of the fault in both Epoch 1 and Epoch 2, as shown in Figures 2d and 3d, considering what has recently appeared in the geophysical literature, showing a correlation between variations of the Earth's rotation speed and seismicity (e.g., Bendick & Bilham, 2017).

Temporal changes in attenuation associated with the 2004 *M*6 Parkfield earthquake have previously been investigated by Kelly et al. (2013), who analyzed anomalies of $t^* = \int_0^L \frac{\pi f}{\beta Q(f)} dl$ (the integral is along the propagation path), and found a sudden coseismic increase in attenuation, followed by an exponential decay with time. Kelly et al. (2013) did not look for differences in attenuation between the two sides of the SAF, and no precursory anomalies could be detected on a sampling volume very similar to that of the present study.

Kelly et al. (2013) observed a factor of 3–4 increase in the quantity $1/Q$, between the onset of the Parkfield main shock and three years later (2007.5–2008). In the hypothesis that the geometrical spreading functions obtained by Malagnini and Dreger (2016) did not change with time on both sides of the SAF, a frequency-dependent increase of $1/Q$ may be calculated from our results as a consequence of the 2004 Parkfield earthquake (Figure S4), with amplitudes and durations in agreement to what described by Kelly et al. (2013). Two different geometrical spreading functions were calculated by Malagnini and Dreger (2016), one for each side of the SAF.

It is important to stress that we are able to maximize the accuracy of our measurements in several ways. First, based on the theoretical results provided by RVT (Cartwright & Longuet-Higgins, 1956; Malagnini & Dreger, 2016; Malagnini & Munafò, 2017; Munafò et al., 2016), we use peak values of narrow band-pass-filtered time histories derived from the original seismograms, instead of the noisier Fourier amplitudes. Second, we exploit the main characteristic of the repeating earthquakes recorded by the HRSN, that is the fact that their seismograms are generated by ruptures that occur several times on the exact same strong fault patch, so that all the seismic sources of a given family of repeaters are essentially co-located in space. Third, we apply a bootstrap approach to the inversion technique, reducing the statistical uncertainties of the attenuation time histories. Finally, the HRSN is a borehole network, and its noise level is very low.

Because we use hypocentral distances shorter than 12 km, and we compute ratios with a reference hypocentral distance of only 4 km, the frequency variations shown here must be related mostly to changes in the

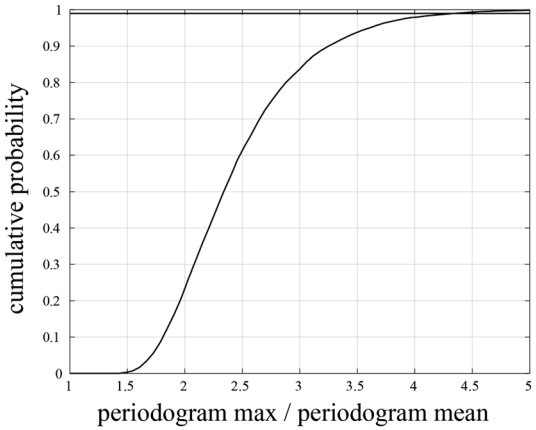

Figure 6. Test for statistical significance. Cumulative distribution of the test statistics to assess statistical significance of the highest periodogram peak. The horizontal line corresponds to a probability of 0.99.

material properties of rocks within the SAF damage zone. In fact, also due to their depths, many of the travel paths of the seismic waves we analyzed are subparallel to the fault, which contributes to limiting the sampled volume to the close vicinity of the SAF.

About the statistical significance of the periodograms, we test the hypothesis that the appearance of the highest peak in a periodogram is statistically significant, and proceed as follows. The statistics considered is P_{max}/P_{mean}, that is, of the ratio between the maximum value of a periodogram and its average value. The cumulative distribution of such statistics under the null hypothesis that the attenuation signal is white Gaussian noise has been computed numerically by means of a simulation sample with 10,000 units (Figure 6). No changes are observed when sample size is increased further.

There is no influence of the white noise variance on this distribution. As an example, we apply the test to the highest peak of each of the four average periodograms for Epoch 1 in Figure S2a, obtaining a p value smaller than 10^{-3} in all cases. In principle, we could apply the test also to the lower peaks after performing an analogous simulation. Finally, the locations of most of these peaks correspond very well to physical tides (the 14.2 months polar tide, or multiples and submultiples of the revolution period of either the Earth around the Sun or the Moon around the Earth), making it very unlikely that their presence is due to random fluctuations.

6. Conclusions

Our results may be summarized as follows:

1. Seismic attenuation is not constant over time, and instead, it fluctuates with clear periodicities indicating a sensitivity to seasonal hydrological loads and polar tides.
2. Whereas the results obtained before the Parkfield earthquake showed seasonal attenuation periodicity, after the main shock we found additional periodicities, including at the period of the 14-day fortnightly solid Earth tide and its harmonics, as well as a period coincident with that of the 14.2-month Chandler wobble or polar tide.
3. The attenuation time histories on the two sides of the SAF show very different behaviors that at times are mirror-like. This is explained in terms of the different behavior of compressive loading and unloading through the evolution of the seismic cycle.
4. Tidal (polar) and seasonal stress perturbations are very small at the depth of the earthquakes on the SAF, roughly between ~100 Pa and ~1 kPa (Johnson et al., 2017), respectively, indicating a strong sensitivity of attenuation to stress. Because of this strong sensitivity to external stresses, we need to explore the possibility that attenuation measurements can be used for understanding the state of stress of the rocks surrounding an active fault, including the recognition of a prefailure critical state.
5. At high frequencies, attenuation time histories show immediate coseismic attenuation changes associated with the 2003 San Simeon earthquake, and with the 2004 Parkfield event, with opposite signs on the two sides of the SAF. This mirrored response across the fault is in opposite sign to the mirrored response in the preevent period.
6. The increasing attenuation trend observed at high frequency before the San Simeon earthquake, which appears to be related to stress accumulation toward the end of the seismic cycle on the SAF, just before the $M6$ Parkfield earthquake of 2004, may indicate that the fault is getting close to failure, but lacks specific information on when the earthquake will occur.
7. Changes in seismic attenuation, before and after the Parkfield earthquake, show opposite signs on the two sides of the SAF. After about four years from the main shock we observe changes is seismic attenuation, with the same sign on both sides of the fault. The fact that late postseismic periods show decreasing attenuation on both sides of the SAF suggests healing is the dominant process.
8. In the crustal volume sampled by the HRSN, earthquake-induced damage from the 2004 Parkfield main shock increases the sensitivity of seismic attenuation to periodic stress fluctuations.

Appendix A

A1. Obtaining RVT-Based Measurements of Relative Amplitudes

Given $a(t)$, a stationary random time history of length T, Random Vibration Theory (RVT; Cartwright & Longuet-Higgins, 1956) may be used to relate to its peak value:

$$peak(a(t)) \approx \zeta a_{RMS} \tag{A1}$$

where the a_{RMS} is its RMS-value calculated over T and ζ may be calculated using the spectral moments of the filtered time history ($\zeta = \zeta(m_0, m_2, m_4)$; see Cartwright & Longuet-Higgins, 1956 ; Malagnini et al., 2000). Given equation (A1) and the Parseval theorem, it can be shown (Malagnini et al., 2000; Malagnini & Dreger, 2016) that the Convolution Theorem may be applied to peak values of the ground motions, if they come from narrowband-filtered time histories.

In fact, a sufficiently narrow band-pass filter guarantees enough stationarity, and yet the presence of a clear peak. Relatively to a band centered on a specific sampling frequency f_c, we obtain such a filter by the application of an eight-pole low-pass Butterworth filter with corner at $\sqrt{2}f_c$, followed by an eight-pole high-pass Butterworth filter with corner at $\frac{f_c}{\sqrt{2}}$ (Malagnini et al., 2000; Raoof et al., 1999). A band-pass filter with the described characteristics is also narrow enough to avoid large variations of the Fourier spectral amplitudes within the filter's corner frequencies (Cartwright & Longuet-Higgins, 1956; Malagnini et al., 2000).

For a narrowband-filtered time history, excited by the *i*th earthquake, and recorded at the *j*th site, RVT allows the following linear relationship:

$$PEAK_{ij}(f) = \log_{10}\left(peak_{ij}(f)\right) = SRC_i(f) + D\left(r_{ij}, r_0, f\right) + SITE_j(f) \tag{A2}$$

Before the inversion, the matrix described by equation (A2) needs to be stabilized by the application of at least two constraints: one on the site terms and one on the path term. In the present study the constraints are the following: (i) null summation of the horizontal components of all sites; (ii) null path term (in log units) at a fixed, arbitrary reference hypocentral distance; and (iii) a minimum roughness constraint for the propagation term $D(r, r_0, f)$ (not in rigorous terms, since the term $D(r, r_0, f)$ is usually unevenly sampled as a function of hypocentral distance).

About constraint (iii), following Yazd (1993), we parameterize $D(r, r_0, f)$ in equation (A2) as a piecewise continuous linear function with N_{nodes} nodes:

$$D(r, r_0, f) = \sum_{j=1}^{N_{\text{nodes}}} L_j(r) D_j(f), \tag{A3}$$

where

$$D(r = r_0, f) = 0, \tag{A4}$$

and

$$L_j = \begin{cases} \frac{r - r_{j-1}}{r_j - r_{j-1}} & \text{if } r_{j-1} \le r \le r_j \\ \frac{r_{j+1} - r}{r_{j+1} - r_j} & \text{if } r_j \le r \le r_{j+1} \\ 0 & \text{otherwise} \end{cases} \tag{A5}$$

Constraint (iii) is finally forced onto the path term at each specific frequency, by requiring

$$D_{j-1}(f) - 2D_j(f) + D_{j+1}(f) = 0. \tag{A6}$$

In case of evenly spaced spatial sampling, constraint (A6) may be described in terms of minimum roughness.

All details of the method highlighted here are described by Raoof et al. (1999), Malagnini and Dreger (2016), and Malagnini et al. (2000). Relative amplitudes of Figures 2–4 are calculated by taking the ratios between the path term at 12 km (best-sampled hypocentral distance) and at the reference distance of 4 km (shortest well-sampled hypocentral distance).

Our analysis is performed on a window of N consecutive events, shifted of one event along time. Adjacent windows overlap by $N-1$ events. In fact, in order to maximize the resolution of the time histories plotted in Figure 3 of the main article, the window is moved with time by one-event steps. The median origin time of the events in the nth time window is assigned to that window. Results shown in this paper have been obtained with $N = 40$, which is the minimum to obtain stable results (we tried $N = 60$, $N = 40$, and $N = 30$: whereas results from $N = 30$ were unacceptably unstable, the San Simeon earthquake-related variations became very small with $N = 60$. $N = 40$ was the best compromise between resolution and stability). A bootstrap approach is carried out by obtaining 10 realizations of each regression, at all frequencies (before each realization we remove 10% of the events), and the 10 different results are averaged together.

The time resolution of our technique depends on the number of earthquakes. After the 2004 main shock, resolution is very high (individual earthquakes are spaced by minutes to hours), but the resolution during Epoch 1 may be on the order of months. About the different resolutions (in terms of periods) of the spectrograms of Figures 2 and 3, the x axes of the figures actually show the two entire sets of available periods. The deep blue portions of Figures 2c and 2d show no energy at the shortest periods.

Finally, a clarification of the meaning of the source terms, because seismic sources (i.e., earthquakes) and source terms are two distinct items, and should be regarded as such. In an environment of varying attenuation, although the individual earthquake is obviously the same, its source term calculated in two different time windows will necessarily be different. The two different realizations, in fact, represent the amplitudes that would be recorded at the same reference hypocentral distance (not at zero distance) in the two different crustal volumes (because attenuation has changed over time). The closer we approach a null reference distance, the less variations we are to expect between the different source terms of one specific earthquake.

To document the changes in source and site terms that occur throughout all the regressions, we added two figures in the supporting information, Figures S5 and S6, that refer to the Pacific and the North American side of the SAF, respectively, during the more interesting Epoch 2. From these plots we see that, on the one hand, source terms fluctuate mildly and smoothly through the entire sequences in which they are inverted, and fluctuations are generally unrelated to the ones of the amplitude ratios of Figure 3 (captions of Figures S5 and S6 provide details). Individual site terms, on the other hand, are very smooth and flat, their average showing a minimal fluctuation. The behaviors of source and site terms during Epoch 1 are very similar to what shown in Figures S5 and S6.

A2. Periodogram Analysis for Unevenly Spaced Time Histories

Let us consider a time series represented by the vector $Y = (y_1, \ldots, y_n)$, where $y_i = s(t_i)$ is the signal sampled at the time $t_i, i = 1, \ldots, n$. Differently from the classical periodograms based on Fourier transform, here the sampling times are unevenly spaced, since they correspond to earthquake occurrences. Then, the Lomb and Scargle periodogram weight at period λ can be computed as (Lomb, 1978; Scargle, 1982)

$$P_{LS}(\lambda) = \frac{\left(\sum_{i=1}^{n} y_i \cos([2\pi/\lambda]\cdot(t_i - \tau(\lambda)))\right)^2}{\sum_{i=1}^{n} cos([2\pi/\lambda]\cdot(t_i - \tau(\lambda)))^2} + \frac{\left(\sum_{i=1}^{n} y_i \sin([2\pi/\lambda]\cdot(t_i - \tau(\lambda)))\right)^2}{\sum_{i=1}^{n} \sin([2\pi/\lambda]\cdot(t_i - \tau(\lambda)))^2}, \tag{A7}$$

where

$$\tau(\lambda) = \frac{\lambda}{4\pi} \arctan\left(\frac{\sum_{i=1}^{n} \sin([4\pi/\lambda]\cdot t_i)}{\sum_{i=1}^{n} \cos([4\pi/\lambda]\cdot t_i)}\right). \tag{A8}$$

The values of the period $\lambda_j, j = 1, \ldots, m$ are chosen here in such a way that, after logarithmic transformation, they are evenly spaced between 2 and $(t_n - t_1)/2$ days.

For each frequency $f_i, i = 1, \ldots, 20$, between 2 and 50 Hz, from $Y(f_i)$ we compute the periodogram $P_{LS}(f_i, \lambda_j)$ at all periods. In order to increase regularity, we apply a nonparametric smoothing along both variables (first on λ, and then on f) based on the Nadaraya-Watson kernel estimator (Eubanks, 1999):

$$P'_{LS}(f_i,\lambda_j)=\frac{\sum_{k=1}^{m}P_{LS}(f_i,\lambda_k)K\left(\left(\log(\lambda_k)-\log(\lambda_j)\right)/h_\lambda\right)}{\sum_{k=1}^{m}K\left(\left(\log(\lambda_k)-\log(\lambda_j)\right)/h_\lambda\right)}\quad j=1,...,m \tag{A9}$$

$$\widetilde{P}_{LS}(f_i,\lambda_j)=\frac{\sum_{k=1}^{20}P'_{LS}(f_k,\lambda_j)K\left(\left(\log(f_k)-\log(f_i)\right)/h_f\right)}{\sum_{k=1}^{20}K\left(\left(\log(f_k)-\log(f_i)\right)/h_f\right)}\quad i=1,...,20, \tag{A10}$$

where the kernel $K()$ function used here is the standardized Gaussian.

A3. Estimating the Smoothing Parameters for the Periodograms (Figures 2c, 2d, 3c, and 3d)

To estimate the smoothing parameter h in the Nadaraya-Watson estimator (Hastie & Tibshirani, 1990, and references therein), different criteria may be used. Among them, there are the Mallows criterion and the "leave-one-out" cross validation (Hastie & Tibshirani, 1990, and references therein). However, the first one needs an estimate for the data noise variance, whereas both of them, although to different degrees, may suffer for undersmoothing.

Here we propose a new criterion based on the maximization of the product p of the linear correlation coefficient between the data y_i and the estimated $\widehat{y}_i$ sequences ($i=1,\dots,n$), times that between the data y_i and the residuals $r_i=\widehat{y}_i-y_i$ ($i=1,\dots,n$):

$$p(h)=\frac{\langle(y-\langle y\rangle)(\widehat{y}-\langle\widehat{y}\rangle)\rangle}{\sqrt{\langle(y-\langle y\rangle)^2\rangle\left\langle(\widehat{y}-\langle\widehat{y}\rangle)^2\right\rangle}}\times\frac{\langle(y-\langle y\rangle)(r-\langle r\rangle)\rangle}{\sqrt{\langle(y-\langle y\rangle)^2\rangle\langle(r-\langle r\rangle)^2\rangle}} \tag{A11}$$

where $<>$ indicates the arithmetic mean. We notice that the first factor reaches the maximum possible value 1 for $h=0$, for which we have $\widehat{y}_i=y_i$ ($i=1,\dots,n$). The value of this factor decreases toward zero as the value of h increases toward infinity.

The maximum possible value 1 is reached asymptotically by the second factor when h tends to infinity, for which we have $\widehat{y}_i=\langle y\rangle$, and $r_i=y_i-\langle y\rangle$ ($i=1,\dots,n$). The value of the second factor decreases toward zero when h approaches zero. Therefore, $p(h)$ approaches zero for very small or very large values of h. By maximizing p, we aim to find a good compromise between the data fidelity and the degree of smoothness of the estimate $\widehat{y}_i=(i=1,...,n)$.

We compute different estimates for different values of h in a finite set of evenly spaced values. Within the set of possible values, we select the optimal value of h that maximizes $p(h)$. In practice, due to the different ranges of values for the two factors of p for the different values used for h, we separately standardize between zero and one the values of the two factors.

In order to obtain each one of the average periodograms, we first average the noisy Lomb-Scargle periodograms for the attenuation sequences of a given cluster, and compute a smooth version of the average periodogram corresponding to an optimal value of h.

We obtain each of the four images (in Figures 2c, 2d, 3c, and 3d of the main text) as follows. We first estimate the optimal value $h_i$for each of the 20 Lomb-Scargle noisy periodograms, and calculate the smoothed version of these periodograms by using the same value of h, equal to the average value of the individual values $h_1,\dots,h_{20}$. We estimated the optimal values h_i' for each of n pseudo-periodograms composed by the 20 values of the above smoothed periodograms corresponding to n different periods. The image is obtained by applying nonparametric smoothing to each one of the n pseudo-periodograms with the same value of h, equal to the average value of these last values $h_1',...,h_n'$.

Acknowledgments
Data for this study come from the High Resolution Seismic Network (HRSN), doi: 10.7932/HRSN, operated by the UC Berkeley Seismological Laboratory, which is archived at the Northern California Earthquake Data Center (NCEDC), doi: 10.7932/NCEDC, http://www.ncedc.org/hrsn/. L.M. and I.M. were partially supported by Ministero dell'Istruzione, dell'Università e della Ricerca (MIUR) under project 0865.020 FISR 2016: "Understanding the nature of time-dependent velocity and attenuation anomalies observed during recent seismic sequences of the central Apennines." All other authors gave their contributions without being supported by specific funds. The authors thank the two anonymous reviewers for their thoughtful comments and suggestions. The authors declare that they have no conflicts of interest. Some figures were built using the Generic Mapping Tools v.4.2.1 (www.soest.hawaii.edu/gmt; Wessel & Smith, 1998).

References

Aron, A., & Hardebeck, J. L. (2009). Seismicity rate changes along the central California coast due to stress changes from the 2003 *M* 6.5 San Simeon and 2004 *M* 6.0 Parkfield earthquakes. *Bulletin of the Seismological Society of America*, *99*(4), 2280–2292. https://doi.org/10.1785/0120080239

Bendick, R., & Bilham, R. (2017). Do weak global stresses synchronize earthquakes? *Geophysical Research Letters*, *44*, 8320–8327. https://doi.org/10.1002/2017GL074934

Bodin, P., Malagnini, L., & Akinci, A. (2004). Ground motion scaling in the Kachchh Basin, India, deduced from aftershocks of the 2001 M_w 7.6 Bhuj earthquake. *Bulletin of the Seismological Society of America*, *94*(5), 1658–1669. https://doi.org/10.1785/012003202

Brenguier, F., Campillo, M., Hadziioannou, C., Shapiro, N. M., Nadeau, R. M., & Larose, E. (2008). Postseismic relaxation along the San Andreas Fault at Parkfield from continuous seismological observations. *Science*, *321*(5895), 1478–1481. https://doi.org/10.1126/science.1160943

Cartwright, D. E., & Longuet-Higgins, M. S. (1956). The statistical distribution of the maxima of a random function. *Proceedings of the Royal Society of London. Series A. Mathematical and Physical Sciences*, *237*, 212–232.

Efron, B. (1981). Nonparametric estimates of standard error: The jackknife, the bootstrap and other methods. *Biometrika*, *68*(3), 589–599. https://doi.org/10.2307/2335441

Eubanks, R. L. (1999). *Nonparametric regression and spline smoothing*. New York: CRC Press.

Gupta, I. N. (1973). Dilatancy and premonitory variations of *P*, *S* travel times. *Bulletin of the Seismological Society of America*, *63*(3), 1157–1161.

Hastie, T. J., & Tibshirani, R. J. (1990). *Generalized additive models*. Boca Raton, FL: Chapman & Hall/CRC.

Hawthorne, J. C., & Rubin, A. M. (2010). Tidal modulation of slow slip in Cascadia. *Journal of Geophysical Research*, *115*, B09406. https://doi.org/10.1029/2010JB007502

HRSN (2014). High Resolution Seismic Network. UC Berkeley Seismological Laboratory. Dataset. doi:https://doi.org/10.7932/HRSN.

Johanson, I. A., & Bürgmann, R. (2010). Coseismic and postseismic slip from the 2003 San Simeon earthquake and their effects on backthrust slip and the 2004 Parkfield earthquake. *Journal of Geophysical Research*, *115*, B07411. https://doi.org/10.1029/2009JB006599

Johnson, C. W., Fu, Y., & Bürgmann, R. (2017). Stress models of the annual hydrospheric, atmospheric, thermal, and tidal loading cycles on California faults: Perturbation of background stress and changes in seismicity. *Journal of Geophysical Research: Solid Earth*, *122*, 10,605–10,625. https://doi.org/10.1002/2017JB014778

Johnson, K. M., Shelly, D. R., & Bradley, A. M. (2013). Simulations of tremor-related creep reveal a weak crustal root of the San Andreas Fault. *Geophysical Research Letters*, *40*, 1300–1305. https://doi.org/10.1002/grl.50216

Kaproth, B. M., & Marone, C. (2013). Slow earthquakes, preseismic velocity changes, and the origin of slow frictional stick–slip. *Science*, *341*(6151), 1229–1232. https://doi.org/10.1126/science.1239577

Kelly, C. M., Rietbrock, A., Faulkner, D. R., & Nadeau, R. M. (2013). Temporal changes in attenuation associated with the 2004 *M*6.0 Parkfield earthquake. *Journal of Geophysical Research: Solid Earth*, *118*, 630–645. https://doi.org/10.1002/jgrb.50088

Khoshmanesh, M., & Shirzaei, M. (2018). Episodic creep events on the San Andreas Fault caused by pore pressure variations. *Nature Geoscience*, *11*(8), 610–614. https://doi.org/10.1038/s41561-018-0160-2

Korneev, V. A., Nadeau, R. M., & McEvilly, T. V. (2003). Seismological studies at Parkfield IX: Fault-zone imaging using guided wave attenuation. *Bulletin of the Seismological Society of America*, *93*(4), 1415–1426. https://doi.org/10.1785/0120020114

Langbein, J., Borcherdt, R., Dreger, D. S., Fletcher, J., Hardebeck, J. L., Hellweg, M., et al. (2005). Preliminary report on the 28 September 2004, *M* 6.0 Parkfield, California earthquake. *Seismological Research Letters*, *76*(1), 10–26. https://doi.org/10.1785/gssrl.76.1.10

Li, Y. G., Vidale, J. E., & Cochran, E. S. (2004). Low-velocity damaged structure of the San Andreas Fault at Parkfield from fault zone trapped waves. *Geophysical Research Letters*, *31*, L12S06. https://doi.org/10.1029/2003GL019044

Lomb, N. R. (1978). The decline of the beta *Canis majoris* pulsation in alpha Virginis. *Monthly Notices of the Royal Astronomical Society*, *185*(2), 325–333. https://doi.org/10.1093/mnras/185.2.325

Madras, N. (2001). Lecture notes on Monte Carlo methods, Fields Institute Monographs, American Mathematical Society, ISBN10 0821829785, ISBN13 9780821829783, 103 pp.

Malagnini, L., Akinci, A., Mayeda, K., Munafò, I., Herrmann, R. B., & Mercuri, A. (2011). Characterization of earthquake-induced ground motion from the L'Aquila seismic sequence of 2009, Italy. *Geophysical Journal International*, *184*(1), 325–337. https://doi.org/10.1111/j.1365-246X.2010.04837.x

Malagnini, L., & Dreger, D. S. (2016). Generalized free-surface effect and random vibration theory: A new tool for computing moment magnitudes of small earthquakes using borehole data. *Geophysical Journal International*, *206*(1), 103–113. https://doi.org/10.1093/gji/ggw113.

Malagnini, L., Herrmann, R. B., & Di Bona, M. (2000). Ground motion scaling in the Apennines (Italy). *Bulletin of the Seismological Society of America*, *90*(4), 1062–1081. https://doi.org/10.1785/0119990152

Malagnini, L., & Munafò, I. (2017). M_w's of seismic sources under thick sediments. *Bulletin of the Seismological Society of America*, *107*(3), 1413–1420. https://doi.org/10.1785/0120160243

Munafò, I., Malagnini, L., & Chiaraluce, L. (2016). On the relationship between M_w and M_L for small earthquakes. *Bulletin of the Seismological Society of America*, *106*(5), 2402–2408. https://doi.org/10.1785/0120160130

Murray, J., & Langbein, J. (2006). Slip on the San Andreas Fault at Parkfield, California, over two earthquake cycles, and the implications for seismic hazard. *Bulletin of the Seismological Society of America*, *96*(4B), S283–S303. https://doi.org/10.1785/0120050820

Nadeau, R. M., & Johnson, L. R. (1998). Seismological studies at Parkfield VI: Moment release rates and estimates of source parameters for small repeating earthquakes. *Bulletin of the Seismological Society of America*, *88*, 790–814.

Nadeau, R. M., & McEvilly, T. V. (2004). Periodic pulsing of characteristic microearthquakes on the San Andreas Fault. *Science*, *303*(5655), 220–222. https://doi.org/10.1126/science.1090353

Nakata, R., Naoki, S., & Tsuruoka, H. (2008). Non-volcanic tremor resulting from the combined effect of Earth tides and slow slip events. *Nature Geoscience*, *1*(10), 676–678. https://doi.org/10.1038/ngeo288

Niu, F., Silver, P. G., Daley, T., Cheng, X., & Majer, E. L. (2008). Preseismic velocity changes observed from active source monitoring at the Parkfield SAFOD drill site. *Nature*, *454*(7201), 204–208. https://doi.org/10.1038/nature07111

Nur, A. (1972). Dilatancy, pore fluids, and premonitory variations of t_s/t_p travel times. *Bulletin of the Seismological Society of America*, *62*, 1217–1222.

O'Connell, R. J., & Budiansky, B. (1977). Viscoelastic properties of fluid-saturated cracked solids. *Journal of Geophysical Research*, *82*(36), 5719–5735. https://doi.org/10.1029/JB082i036p05719

Pollitz, F. F., Wech, A., Kao, H., & Bürgmann, R. (2013). Annual modulation of non-volcanic tremor in northern Cascadia. *Journal of Geophysical Research: Solid Earth*, *118*, 2445–2459. https://doi.org/10.1002/jgrb.50181

Raoof, M., Herrmann, R. B., & Malagnini, L. (1999). Attenuation and excitation of three-component ground motion in Southern California. *Bulletin of the Seismological Society of America*, *89*, 888–902.

Scargle, J. D. (1982). Studies in astronomical time series analysis. II—Statistical aspects of spectral analysis of unevenly spaced data. *Astrophysical Journal*, *263*, 835–853. https://doi.org/10.1086/160554

Scholz, C. (2019). *The mechanics of earthquakes and faulting*. Cambridge: Cambridge University Press. https://doi.org/10.1017/9781316681473

Takano, T., Nishimura, T., Nakahara, H., Ohta, Y., & Tanaka, S. (2014). Seismic velocity changes caused by the Earth tide: Ambient noise correlation analyses of small-array data. *Geophysical Research Letters*, *41*, 6131–6136. https://doi.org/10.1002/2014GL060690

Thomas, A. M., Bürgmann, R., Shelly, D. R., Beeler, N. M., & Rudolph, M. L. (2012). Tidal triggering of low frequency earthquakes near Parkfield, CA: Implications for fault mechanics within the brittle-ductile transition. *Journal of Geophysical Research*, *117*, B05301. https://doi.org/10.1029/2011JB009036

Thomas, A. M., Nadeau, R. M., & Bürgmann, R. (2009). Tremor-tide correlations and near-lithostatic pore pressure on the deep San Andreas Fault. *Nature*, *462*(7276), 1048–1051. https://doi.org/10.1038/nature08654

Thurber, C., Zhang, H., Waldhauser, F., Hardebeck, J., Michael, A., & Eberhart-Phillips, D. (2006). Three-dimensional compressional wavespeed model, earthquake relocations, and focal mechanisms for the Parkfield, California, Region. *Bulletin of the Seismological Society of America*, *96*(4B), S38–S49. https://doi.org/10.1785/0120050825

Titus, S. J., Dyson, M., DeMets, C., Tikoff, B., Rolandone, F., & Bürgmann, R. (2011). Geologic versus geodetic deformation adjacent to the San Andreas Fault, central California. *Bulletin of the Seismological Society of America*, *123*(5-6), 794–820. https://doi.org/10.1130/B30150.1

Turner, R. C., Shirzaei, M., Nadeau, R. M., & Bürgmann, R. (2015). Slow and Go: Pulsing slip rates on the creeping section of the San Andreas Fault. *Journal of Geophysical Research: Solid Earth*, *120*, 5940–5951. https://doi.org/10.1002/2015JB011998

Uchida, N., & Bürgmann, R. (2019). Repeating earthquakes. *Annual Review of Earth and Planetary Sciences*, *47*(1), 305–332. https://doi.org/10.1146/annurev-earth-053018-060119

Van der Elst, N. J., Delorey, A. A., Shelly, D. R., & Johnson, P. A. (2016). Fortnightly modulation of San Andreas tremor and low-frequency earthquakes. *Proceedings of the National Academy of Sciences*, *113*(31), 8601–8605. https://doi.org/10.1073/pnas.1524316113

Vasseur, J., Wadsworth, F. B., Heap, M. J., Main, I. G., Lavallée, Y., & Dingwell, D. B. (2017). Does an inter-flaw length control the accuracy of rupture forecasting in geological materials? *Earth and Planetary Science Letters*, *475*, 181–189. https://doi.org/10.1016/j.epsl.2017.07.011

Waldhauser, F., & Schaff, D. P. (2008). Large-scale relocation of two decades of Northern California seismicity using cross-correlation and double-difference methods. *Journal of Geophysical Research*, *113*, B08311. https://doi.org/10.1029/2007JB005479

Wang, Q.-Y., Brenguier, F., Campillo, M., Lecointre, A., Takeda, T., & Aoki, Y. (2017). Seasonal crustal seismic velocity changes throughout Japan. *Journal of Geophysical Research: Solid Earth*, *122*, 7987–8002. https://doi.org/10.1002/2017JB014307

Wessel, P., & Smith, W. H. F. (1998). New, improved version of generic mapping tools released. *Eos Transactions AGU*, *79*(47), 579. https://doi.org/10.1029/98EO00426

Winkler, K., & Nur, A. (1972). Pore fluids and seismic attenuation in rocks. *Geophysical Research Letters*, *6*(1), 1–4. https://doi.org/10.1029/GL006i001p00001

Winkler, K., Nur, A., & Gladwin, M. (1979). Friction and seismic attenuation in rocks. *Nature*, *277*(5697), 528–531. https://doi.org/10.1038/277528a0

Yazd, M. R. S. (1993). Ground motion studies in the Southern Great Basinof Nevada and California, Ph.D. Thesis, Saint Louis University.

Zoback, M. D., Hickman, S. H., & Ellsworth, W. L. (2010). Scientific drilling into the San Andreas Fault zone. *EOS, Transactions American Geophysical Union*, *91*(22), 197–199. https://doi.org/10.1029/2010EO220001

References From the Supporting Information

Ward, J. H. (1963). Hierarchical grouping to optimize an objective function. *Journal of the American Statistical Association*, *58*, 234–244.